Journal of Catalysis 457 (2026) 116817

Contents lists available at ScienceDirect

Journal of Catalysis

journal homepage: www.elsevier.com/locate/jcat

Research article

Formaldehyde formation and its impact on the MTO initiation investigated with *ab initio* molecular dynamics simulations[☆]

Hector Vicente [a,b], Philipp N. Plessow [a,*]

[a] *Karlsruhe Institute of Technology, Institute of Catalysis Research and Technology, Hermann-von-Helmholtz-Platz 1, Eggenstein-Leopoldshafen, 76344, Germany*
[b] *University of the Basque Country, Department of Chemical Engineering, Barrio Sarriena s/n, Leioa, 48940, Spain*

ARTICLE INFO

Keywords:
Zeolite
Reaction mechanism
Theory
DFT

ABSTRACT

Formaldehyde plays an important role in the methanol to olefins (MTO) process as a hydrogen-acceptor and also as a precursor to carbon monoxide. Therefore, it is discussed both as a central intermediate in the initiation of the MTO process as well as during deactivation. Here, we compute activation barriers for hydrogen transfer reactions that eventually yield formaldehyde and CH_4 from the reaction of DME or methanol and a surface methoxy species (SMS). Analogous reactions lead to the formation of CO from formaldehyde. Using the intermediate hard sphere model, we compute anharmonic adsorption free energies and then apparent free energies using molecular dynamics (MD) simulations. Additionally, we perform high level electronic structure calculations using the random phase approximation (RPA) evaluated with free energy perturbation theory (FEPT). Together with recently reported methylation barriers for CO and ketenes, this provides highly accurate barriers for the initiation of the MTO process via the CO-catalyzed mechanism. Combining the data provides a seamless Gibbs free energy profile where the kinetically relevant parts – including adsorption – are computed explicitly with MD simulations and corrected with RPA calculations. Formaldehyde formation occurs more readily than the second dehydrogenation step that yields CO, which is thus the rate-limiting step. This analysis is only possible with the availability of anharmonic adsorption free energies at the surface methoxy species. At 400 °C and 1 bar reference pressure adsorption is generally unfavorable in terms of Gibbs free energy for the adsorbates considered.

1. Introduction

The catalytic transformation of methanol into light olefins (MTO) stands as a promising alternative for light olefin production [1–3], and thus a vector for transitioning from a crude oil-based petrochemical industry towards a sustainable one [4,5]. Methanol (MeOH) can be produced from biomass [6,7] or CO_2 hydrogenation [8–11], which would reduce the impact of the pollutant gases emitted from industrial processes and those already present as greenhouse gases in the atmosphere [12,13]. The MTO process employs acidic zeolites as catalysts and the methanol feed or, more precisely, the equilibrium mixture of methanol and dimethyl ether (DME) [14,15], reacts with the hydrocarbon species present in the reaction medium, which are named hydrocarbon pool (HCP) [16–18]. Later works proposed the dual-cycle mechanism to explain the wide range of products formed during MTO [5,19,20]. There is significant interest in improving the MTO process, also through reaching a better understanding of the underlying mechanism [4,21–28].

The mechanism of the initiation of the MTO process has attracted a lot of attention over the past decades [29,30]. The question is how the HCP, consisting of hydrocarbons with C–C bonds is built, when starting from a pristine zeolite and a pure methanol or DME feed. One explanation brought forward is that impurities in the zeolite or in the feed will be sufficient to initiate the hydrocarbon pool [31,32], but the more popular explanation is that there are reaction mechanisms that allow the direct formation of C–C bonds starting from clean methanol or DME. Several mechanisms for this initial C–C bond formation have been proposed over the years and have been investigated both experimentally and theoretically. Experimental investigations mainly rely on the detection of reactive intermediates during the initiation phase. A problem with this approach is that it is usually not clear that a detected intermediate is necessarily involved in the initiation, and thus theoretical investigations are used to support the experimentally observed results.

[☆] This article is part of a Special issue entitled: ‘Molecular Dynamics in Catalysis’ published in Journal of Catalysis.

[*] Corresponding author.

E-mail address: philipp.plessow@kit.edu (P.N. Plessow).

https://doi.org/10.1016/j.jcat.2026.116817
Received 13 January 2026; Received in revised form 20 February 2026; Accepted 6 March 2026

Theoretical investigations typically provide Gibbs free energy profiles for reaction mechanisms. There are several pitfalls in the theoretical investigations, starting from the fact that the most feasible generalized gradient approximation (GGA) functionals, such as PBE, generally predict too low barriers, and mechanisms will therefore appear more favorable than they actually are [33–38]. Additional problems can occur, when no kinetic simulations are performed and instead a rough estimate of the kinetics in terms of the interpretation of barriers is pursued. The latter approach will often result in statements such as "mechanism A is feasible at the investigated conditions" or "mechanism A is more favorable than mechanism B". In such a case, it is best practice to follow the recipe described as the energetic span model [39] and to apply it to Gibbs free energies at the appropriate temperature and reference pressure. The discussion of individual, intrinsic barriers or of activation energies (rather than free energies) is generally insufficient to predict overall kinetics. While these are general issues in computational catalysis, the initiation kinetics are even more complicated. This is because initiation does need to supply a certain rate of product formation as judged by the turn-over-frequency (TOF). In the case of MTO, a sufficient amount of hydrocarbons must be present to start up the hydrocarbon-pool, which will initially only consist of the autocatalytic olefin cycle. It is impossible to decide based on chemical intuition or on the application of the energetic span model, what a reasonable barrier height during initiation is. This will also depend on the kinetics of the autocatalytic olefin cycle. In our kinetic simulations of the initiation process using a batch reactor model, we found that high barriers during initiation are not prohibitive since small amounts of impurities are sufficient to initiate the hydrocarbon pool [32,40].

Most of the mechanisms for the initiation that are still debated have been investigated theoretically by Tajima et al. in 1998 [41]. Among those are the oxonium-ylide and carbene mechanism that are in the current literature no longer proposed as likely mechanisms. The main two candidate mechanisms that have emerged are the methane-formaldehyde mechanism [41] and the CO-catalyzed mechanism [42], see Fig. 1. Both mechanisms have been further investigated and refined since their original proposal. In the methane-formaldehyde mechanism, formaldehyde needs to be formed first, where Tajima et al. proposed a hydride transfer from the CH_3-group of methanol to a surface methoxy species (SMS), thus liberating CH_4 as a byproduct. This is generally still believed to be the most favorable mechanism for creating formaldehyde and is corroborated by the experimental detection of CH_4. The analogous reaction of DME was often found to be somewhat more favorable [43], but requires that DME is first formed from methanol through dehydration. Formaldehyde then reacts with CH_4 to give ethanol, which can subsequently eliminate water to yield ethylene. This requires the reaction of two rare species and is therefore intrinsically unfavorable. Variants of the methane-formaldehyde mechanism have been proposed in which instead of the C-H bond of CH_4, other C-H bonds are attacked [44–46]. The CH_3-groups of methanol and DME were studied by Fan and coworkers [44,45], as they are the most abundant species during initiation. Recently, van Speybroeck and coworkers studied the hydrate, the hemi-acetal and the acetal of formaldehyde that are formed through the reaction of formaldehyde with water or methanol as additional substrates [46]. They concluded that the barriers for these substrates are lower and attributed this to lower C-H bond strengths.

The CO-catalyzed mechanism was first proposed by Jackson and Bertsch in 1990 [42] and later taken up by Tajima et al. [41] At that time no specific proposal regarding the origin of CO was made, but it was speculated that it originates from further oxidation of formaldehyde, which is still accepted as the most likely mechanism. The oxidation of formaldehyde is in principle analogous to its formation from methanol or DME. In one way or another, a hydrogen transfer needs to take place, which is commonly believed to be more facile when transferred to an SMS yielding CH_4. The main difference is that the direct reaction of formaldehyde was found to be rather unfavorable [47]. Instead, the hydrate, hemi-acetal or acetal of formaldehyde ($OHCH_2OH$, $OHCH_2OCH_3$, $CH_3OCH_2OCH_3$) are more reactive, but less stable than formaldehyde in terms of Gibbs free energy. Having formed CO, the CO-catalyzed mechanism proceeds via methylation of CO to ketene, further to methyl ketene and then dimethyl ketene, followed by decarbonylation to propylene [42]. The CO-catalyzed mechanism is similar to SMS carbonylation, or more precisely DME carbonylation, also performed over acidic zeolites, for which acetic acid, in equilibrium with methyl acetate, is the commonly accepted reaction product [48–51]. It should be noted that the latter is performed at 150 to 200 °C, instead of the 350 °C plus used typically for MTO process.

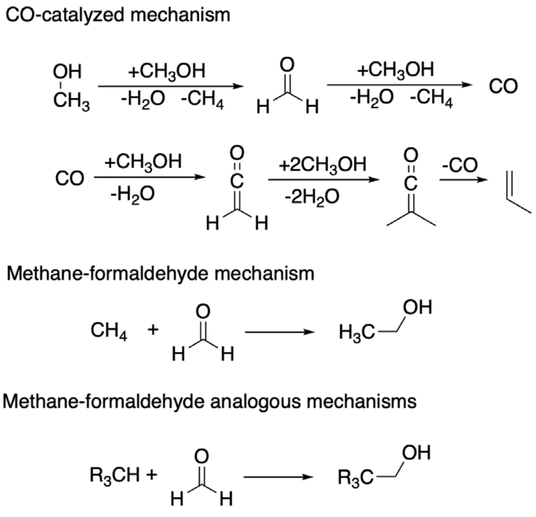

Fig. 1. Overview of selected mechanisms discussed for the initiation of the MTO process.

Both the CO-catalyzed mechanism and the methane-formaldehyde mechanism require that formaldehyde is formed, which is in fact observed frequently [43] also in the form of its acetal, dimethoxy methane (DMM) [46,52]. Methane-formation during initiation has been reported in many experimental studies [43,53–56], although H_2-formation was also observed in a few cases [56–58]. CO is frequently detected [43], as well as surface acetate [52] and methyl acetate [52,56], which can form from ketene and vice versa. Despite being present only in low concentration, both ketene and methyl ketene have been detected [59–61]. The detection of ketenes is usually seen as a confirmation of the CO-catalyzed pathway, but we note here that it is also an intermediate in the methane-formaldehyde related mechanism proposed by van Speybroeck and coworkers [46]. There are also reactants observed during initiation that fit neither to methane-formaldehyde nor to the CO-catalyzed pathway: CO_2[16,43,62] and acetaldehyde [58]. In our theoretical investigations on possible origins of CO_2-formation, we have concluded that coupling of formaldehyde with ketene is more favorable under initiation conditions than ketonic decarboxylation of ketene via acetic acid [63,64].

Formaldehyde also plays an important role in the deactivation of zeolites. After formation through hydrogen-transfer reactions, formaldehyde is believed to engage in the formation of dienes through a Prins reaction, leading eventually to coke formation [62,65–70]. It is also interesting to note that formaldehyde was reported to form in steel reactors without zeolites present [71]. Ketene is another main reactive intermediate and is also being investigated extensively. Besides being an intermediate during initiation, ketene also forms during the syngas-to-olefin and OX/ZEO processes [59,60,72]. Due to this central role, several investigations focus on the reactivity of ketene [61,73–80].

In this work, we use MD simulation with the intermediate hard sphere model (IHSM) [81,82] to compute adsorption free energies of

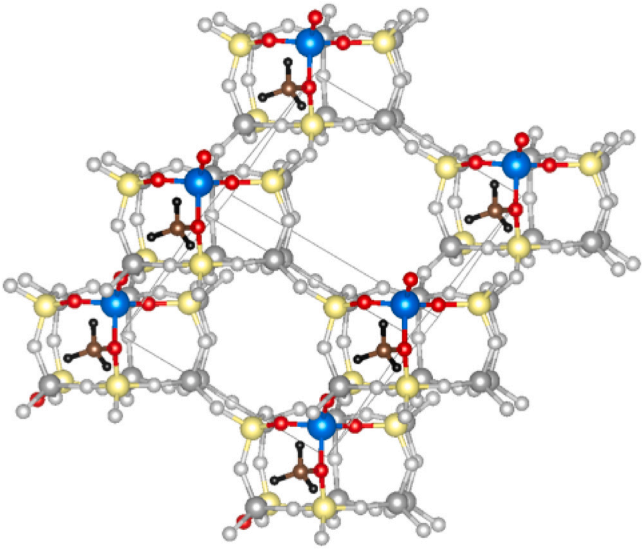

Fig. 2. Atomic structure of the employed primitive cell of chabazite (red = O, black = H, brown = C, blue = Al, yellow = Si, gray = remaining framework). (For interpretation of the references to color in this figure legend, the reader is referred to the web version of this article.)

MeOH, DME, DMM and methyl ketene at SMS. Using blue moon sampling, intrinsic activation free energies are then computed for hydrogen transfer from methanol, DME and DMM to the SMS, generating CH_4 as a byproduct. Together with previous results and static calculations, a complete Gibbs free energy diagram for the initiation pathway of the MTO process is then constructed. Importantly, all crucial parts were computed using MD simulations. All PBE-D3 results are improved using the random phase approximation (RPA), either as single point energy calculations or using free energy perturbation theory (FEPT), for static and MD simulations, respectively.

2. Methods

The primitive cell of CHA with 12 T atoms was employed, with either the proton or the SMS placed at the oxygen commonly labeled O4 that connects two T atoms in the same double six-ring, where one is in the upper and one in the lower six-ring, as depicted in Fig. 2. For CHA, we employ the lattice constants from our previous work [81,82], where the unit cell was optimized for the pristine pure SiO_2-zeolite without symmetry constraints. The same unit cell was used in all calculations, including gas phase species.

All structure optimizations and MD simulations were performed using the PBE functional [83] along with the D3-correction in the zero-damping version [84]. The DFT calculations were performed using the Vienna Ab-Initio program package (VASP) in versions 6.3.0 and 6.4.3 with the projector augmented wave (PAW) method [85–87] and standard PAW potentials and real-space projectors for all PBE calculations. A cutoff of 400 eV was used for the expansion of the wave function in plane waves, and a FFT-grid using lattice vectors with a norm up to 2 times larger than for the wave function, using (PREC = Accurate). The Brillouin zone was sampled only at the Γ-point. This approximation was checked by performing single-point energy calculations using (2 × 2 × 2)-k-point sampling at the PBE-D3 level of theory, see Table S15. The largest observed differences for reaction energies relative to the initial state a are −2.3 kJ mol^{-1} for TS(a-b) and −1.4 kJ mol^{-1} for TS(c-d).

Vibrational analysis was performed by calculating the full Hessian numerically, using central differences with displacements of 0.01 Å. Free energy contributions were obtained on the one hand using the classical harmonic partition function [88] to compare with results from the MD simulations:

$$\Delta G_{\text{harm,class.}} = -k_B T \sum_i \ln\left(\frac{k_B T}{\hbar\omega_i}\right). \tag{1}$$

Here, k_B is the Boltzmann constant, T the temperature, $\hbar$ the reduced Planck constant and ω_i the angular frequency of the harmonic vibration. For the calculation of the final free energy profile, the quantum mechanical partition function was used:

$$\Delta G_{\text{harm,QM}} = -k_B T \sum_i \ln\left(\frac{\exp\left(-\frac{\hbar\omega_i}{2k_B T}\right)}{1-\exp\left(-\frac{\hbar\omega_i}{k_B T}\right)}\right). \tag{2}$$

The total harmonic Gibbs free energy at the PBE-D3 level of theory is then:

$$G_{\text{PBE-D3,harm,QM}} = E_{\text{PBE-D3}} + \Delta G_{\text{harm,QM}} + \Delta G_{\text{rot-trans}} \tag{3}$$

$$G_{\text{PBE-D3,harm,class}} = E_{\text{PBE-D3}} + \Delta G_{\text{harm,class}} + \Delta G_{\text{rot-trans}}, \tag{4}$$

using the QM and classical version of the vibrational harmonic partition function, where $\Delta G_{\text{rot-trans}}$ is the contribution from the rigid-rotator and free translator model.

The blue moon [89–92] simulations were performed at 400 °C using the Andersen thermostat, a collision probability of 0.025, and a time step of 0.5 fs. Constrained simulations with a length of about 90 ps (180,000 steps) were carried out for different values of ξ (see Tables S6 and S7). To calculate adsorption properties, which do not depend on atomic masses, the mass of hydrogen was substituted with that of tritium (3.0 a.u.), and a larger collision probability and time step of 0.05 and 1 fs, respectively, were used. The initiation period for each MD simulation was determined using the Mann–Kendall test, based on the total energy averaged over blocks of 2000 steps [93]. After removing the initiation period, the correlation length was determined using the blocking method [94], again based on the total energy.

To increase the level of accuracy of our calculations we performed RPA (random phase approximation) calculations, using single point energy calculations at stationary points for the harmonic approximation, and FEPT using every 1000th MD-step for the MD simulations. All RPA calculations were performed only at the Γ-point, using well-converged PBE wave functions, with a cubic-scaling version as implemented in VASP [95]. The RPA calculations were also carried out using standard PAW potentials with a cutoff of 400 eV. We used the second-order cumulant expansion of FEPT due to the small number of structures, although we note that results using the full exponential expression differ by less than 1 kJ mol^{-1}, even in terms of total free energies, see Table S10. Using every 1000th MD-step results in 100 to 200 RPA-calculations per step, depending on the specific length and initiation period of the MD. The I_w-index [96] is above 0.10 for all the adsorption and transition state calculations (see Table S10), except for DMM where 0.05 and 0.07 are found for TS and adsorption, respectively. Due to the poorer overlap of the distributions for DMM, additional RPA calculations were performed every 500th step leading to more than 300 energies in this case. The observed change in free energy differences is below 0.6 kJ mol^{-1}. This, as well as an additional summary of free energies obtained from FEPT-calculations employing fewer RPA-calculations, is shown in Tables S11 and S12. Overall, we thus consider the accuracy of the RPA FEPT-calculations and thus the number of underlying RPA-calculations sufficient. Further improvements in sampling would be possible by performing additional calculations or by training machine learning models to the difference between RPA and PBE-D3 and then using these models in FEPT, so called machine learning thermodynamic perturbation theory (MLPT) [96–99].

The harmonic Gibbs free energy used eventually to discuss the reaction mechanisms at 400 °C is obtained as:

$$G_{\text{RPA,harm}} = E_{\text{RPA}} + \Delta G_{\text{harm,QM}} + \Delta G_{\text{rot-trans}}. \tag{5}$$

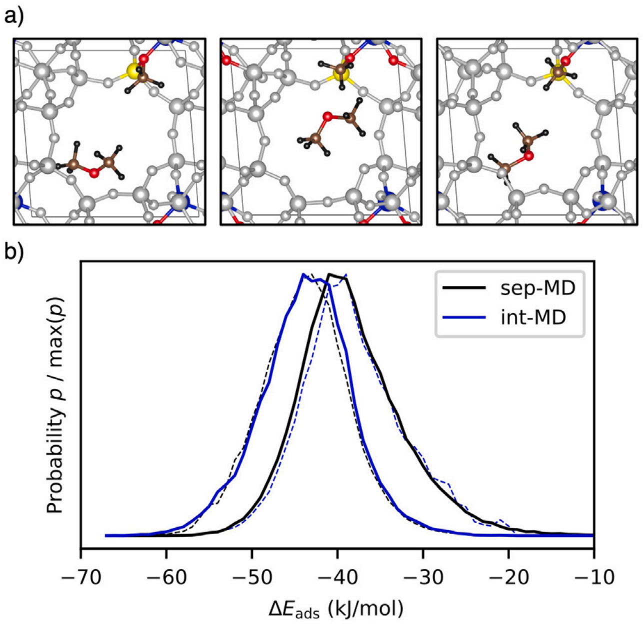

Fig. 3. Adsorption of DME at an SMS at 400 °C. (a) Selected snapshots of the MD trajectory showing the mobility of the adsorbate (red = O, black = H, brown = C, blue = Al, yellow = Si, gray = remaining framework). (b) Probability distributions for the interaction energy (in presence of the IHSM) between zeolite and adsorbate. The probability based on the separate MD simulations (sep-MD) and on the interacting MD (int-MD) are shown. The dashed lines show a histogram that is weighted by the exponential factor of the FEPT-expression. (For interpretation of the references to color in this figure legend, the reader is referred to the web version of this article.)

Here, E_{RPA} is the RPA energy obtained as a single point calculation for the PBE-D3 optimized structure.

Adsorption free energies based on MD simulations were computed using a recently developed approach that employs an intermediate hard sphere model (ISHM) [81,82]. Same as for the Widom test particle method [100–102], the free energies difference between the zeolite with and without adsorbate is computed based on MD-simulations. The hamiltonian for any system can be written as:

$$\mathcal{H} = \mathcal{H}_{\text{sep}} + V, \tag{6}$$

where $\mathcal{H}_{\text{sep}}$ corresponds to the separate hamiltonian of empty zeolite and the adsorbate in the gas phase. The interaction is described by V and is zero in the non-interacting system, and equals V_{int} for the interacting system. In the IHSM-approach an intermediate hard sphere potential V_{IHSM} is introduced to generate intermediate states. The potential acts only between zeolite and adsorbate and is given by:

$$V_{\text{IHSM}} = \sum_{i=1}^{N_{\text{zeolite}}} \sum_{j=1}^{N_{\text{adsorbate}}} V_{\text{IHSM}}^{ij}(r_{ij}). \tag{7}$$

The pairwise atomic distances are r_{ij} and the corresponding hard sphere radii are r_{ij}^{hard}:

$$V_{\text{IHSM}}^{ij}(r_{ij}) = \begin{cases} 0 \text{ if } r_{ij} > r_{ij}^{\text{hard}} \\ \infty \text{ else.} \end{cases} \tag{8}$$

The same large radii were employed as in our previous work [81,82]. The resulting potentials of states 0 (non-interacting), 1, 2 and 3 (fully interacting) are:

$$V_0 = 0 \tag{9}$$

$$V_1 = V_{\text{IHSM}} \tag{10}$$

$$V_2 = V_{\text{int}} + V_{\text{IHSM}} \tag{11}$$

$$V_3 = V_{\text{int}}. \tag{12}$$

In the Widom test particle method, the adsorption free energy is computed directly between states 0 and 3 using forward FEPT based on state 0. This is done in practice based on DFT simulations of the separate empty zeolite and the adsorbate in the gas phase. The energy differences are then computed by combining adsorbate and zeolite structures from both trajectories and evaluating the DFT-energy of the combined structure. A practical issue with this is that there are collisions between adsorbates and zeolites, which need to be dealt with. The IHSM solves this issue, by introducing the intermediate states and decomposing the adsorption free energy into the components:

$$\Delta A_{\text{ads}} = \Delta A_{1\text{-}0} + \Delta A_{2\text{-}1} + \Delta A_{3\text{-}2}. \tag{13}$$

The hard-sphere model effectively removes all structures from the trajectory where zeolite and adsorbate collide. By choosing reasonably high radii, one can additionally remove structures in which the zeolite and adsorbate interact repulsively. The benefit of this is that the central quantity $\Delta A_{2\text{-}1}$, where the actual interacting potential is switched on, is much better defined and has very good overlap between initial and final state (1 and 2). We compute ΔA_{2-1} using Bennett's acceptance ratio method (BAR) [103,104] based on state 1 and 2, although one could also use only forward or backward FEPT.

Evaluating $\Delta A_{1\text{-}0}$ and $\Delta A_{3\text{-}2}$ is trivial and is done based on FEPT using the existing MD trajectories of separate and interacting states (0 and 3):

$$\Delta A_{1\text{-}0} = -k_B T \ln \left\langle \exp\left(-\frac{V_{\text{IHSM}}}{k_B T}\right)\right\rangle_0 \tag{14}$$

$$\Delta A_{3\text{-}2} = +k_B T \ln \left\langle \exp\left(-\frac{V_{\text{IHSM}}}{k_B T}\right)\right\rangle_3 \tag{15}$$

According to Eq. (8), the exponential in Eqs. (14) and (15) is either 0 or 1. For $\Delta A_{1\text{-}0}$, this corresponds simply to a reduction in the accessible volume, starting from state 0, where the adsorbate in the gas phase has the same probability for all positions in the unit cell. For $\Delta A_{3\text{-}2}$, the situation is a bit different, since mainly the part of the trajectory is removed where zeolite and adsorbate interact repulsively.

3. Results and discussion

3.1. Adsorption of MeOH, DME, DMM and methyl ketene

The adsorbates interact generally weakly with the SMS and can rotate and translate freely within the cavity. This free movement is exemplified in Fig. 3(a) for DME. For MeOH and DME, we additionally observed that coordination of the oxygen to the Al atom of the active site occurs for a small part of the trajectory. Due to the rare occurrence, we deem this state insignificant (see Supporting Information for detailed discussion). For analysis we simply employed a continuous part of the MD trajectory, where this coordination does not occur. The results of the calculation of the adsorption free energy using the IHSM-model are shown in Fig. 3 for DME. Fig. 3(a) illustrates the mobility of DME which can access the entire cavity of H-SSZ-13. Fig. 3(b) shows the probability distribution for the adsorption energy in the presence of the IHSM, specifically $V_2 - V_1$. It can be seen that the distributions overlap significantly and are well-behaved. The same is observed for the rest of adsorbates in Fig. S2.

The obtained adsorption free energy values are listed in Table 1, with the anharmonicity values in Table 2, calculated as the differences from the values in Table 1. Additional data for the individual contributions to the adsorption free energy, including error estimates is given in Table S3 in the supporting information. The statistical error based on the BAR method is largest for DMM with 0.3 kJ mol^{-1}. As expected, Table 2 shows that the harmonic approximations generally underbinds, with anharmonicities between −15 and −26 kJ mol^{-1}. At the PBE-D3 level of theory, adsorption free energies range from 0 to 12 kJ mol^{-1}, with the largest adsorbate DMM binding strongest. At the RPA level of theory, binding is weaker, with adsorption free energies between 22 and 24 kJ mol^{-1}.

3.2. Hydrogen transfer from methanol, DME and DMM to a surface methoxy species

The formation of unsaturated hydrocarbons such as formaldehyde during initiation is believed to mainly proceed via the formation of CH_4[43,53–56], although H_2-formation [56–58] is also discussed. The reaction occurs through hydrogen transfer to an SMS, yielding CH_4 and a carbocation that can then quickly react to a more stable neutral species. The transition state in the harmonic approximation is depicted in Fig. 4(a) for the case of DME. The collective variable used to determine the activation free energy is a linear combination of three bond lengths: The CH-distance d_3 of the hydrogen to the carbon of DME, to which it is initially bound, the CH-distance d_2 of the hydrogen to the CH_3-group and the CO-distance between the CH_3-group and the oxygen atom of the zeolite to which it is initially bound. Fig. 4(b) shows a histogram of the collective variable for the initial, adsorbed state, which has a maximum around $\xi = -0.3$ Å. The histograms for the other molecules are displayed in Fig. S4. We choose $\xi_{\mathrm{ref}} = 0$ as a reference point and Fig. 4(c) shows the obtained free energy gradient, its spline interpolation and the free energy curve obtained by integration of the spline. The maximum of the free energy curve is located at $\xi^\ddagger = 2.00$ Å for methanol, $\xi^\ddagger = 1.95$ Å for DME and $\xi^\ddagger = 1.85$ Å for DMM. As described in Ref. [105], the intrinsic free energy barrier is obtained as:

$$\Delta A^\ddagger_{\mathrm{int}} = A(\xi^\ddagger) - A(\xi_{\mathrm{ref}}) - k_B T \ln\left[\frac{h}{k_B T}\frac{\langle \dot{\xi} \rangle_{\xi^\ddagger}}{2} P(\xi_{\mathrm{ref}})\right].$$

The free energy profile of MeOH and DMM is similar to DME and is shown in Fig. S3. Individual contribution to the activation free energies including error estimates are listed in Table S5. The statistical error for the intrinsic activation free energy is largest for DMM with 1.9 kJ mol^{-1}. For DMM, we introduced additional Fermi-type-potentials to suppress side reactions. The side reactions can occur in the transition state region ($\xi \geq 1.4$ Å) and consist of hydrogen transfers from other C-H bonds to the CH_3 group, forming CH_4. This was prevented by adding a repulsive Fermi-type potential for the interaction of the carbon of the CH_3 group with the other hydrogens of DMM, centered at 1.8 Å with a height of 1 eV and a width of FBIAS_D=50. An additional side reaction is the transfer of the CH_3-group to the oxygens of DMM and this was prevented by adding similar potentials, but with a height of 2 eV centered at 2.0 Å.

The choice of the small T12 unit cell is motivated by the fact that it is possible to perform RPA calculations on standard computing facilities. The limitations of using such a small unit cell were tested by comparing static PBE-D3 activation energies for the T12 cell with a (2 × 2 × 1) T48 super cell that contains only one adsorbate, but the same Si/Al ratio, see Fig. S5. The largest difference in barrier height is observed for MeOH, where the barrier is 11.1 kJ mol^{-1} lower in the T12 cell. This can be explained by hydrogen bonding between the OH-group of the reacting methanol and the periodic image of the reacting active site. All other deviation are smaller, but still all barriers are lower for the T12 cell, ranging from a stabilization of 0.5 kJ mol^{-1} for CO to 5.7 kJ mol^{-1} for DME. The error in apparent barriers due to using a small unit cell is thus in all cases smaller than the anharmonicity, although this gets close for MeOH (−11.1 kJ mol^{-1} versus −16.7 kJ mol^{-1}). The error of PBE-D3 versus the RPA is in all cases multiple times larger than that associated with the small unit cell and we therefore consider our calculations accurate despite these limitations.

We will now analyze the source of anharmonicity, giving rise to the observed difference between the results obtained via the MD simulation and the harmonic approximation. For the considered weakly adsorbed species, the adsorbates are translating and rotating in the cavity, which

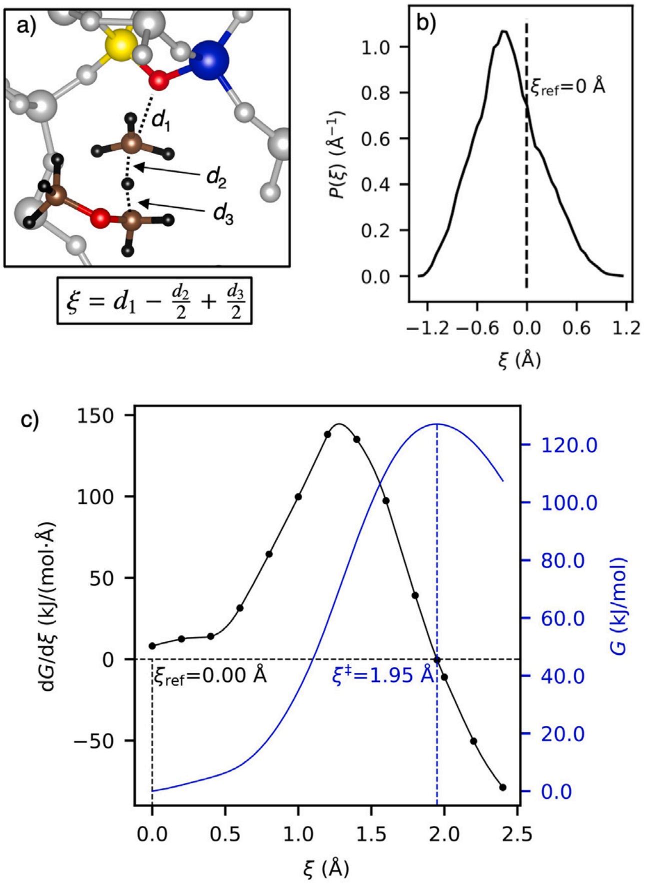

Fig. 4. Calculation of intrinsic activation free energies for hydrogen transfer from DME at 400 °C using the blue moon approach. (a) Transition state for DME (red = O, black = H, brown = C, blue = Al, yellow = Si, gray = remaining framework) (b) Probability distribution of the reaction coordinate ξ of the initial state, with $\xi_{\mathrm{ref}} = 0$ highlighted. (c) Free energy gradient obtained from blue moon sampling, with ξ_{ref} and $\xi^\ddagger$ highlighted. The spline interpolation of the gradient and the free energy profile obtained through integration are also shown. (For interpretation of the references to color in this figure legend, the reader is referred to the web version of this article.)

Table 1
Results of the MD simulations and static calculations with the harmonic approximation for adsorptions and barriers computed in this work at 400 °C, given in kJ mol^{-1}.

Method	Quantity	MeOH	DME	DMM	Methyl ketene
PBE-D3/MD	ΔG_{ads}	11.8	6.8	−0.0	5.9
	$\Delta A^\ddagger_{\mathrm{int}}$	133.4	130.6	121.4	93.5
	$\Delta G^\ddagger_{\mathrm{app}}$	145.2	137.4	121.4	99.5
PBE-D3/harm.[a]	ΔG_{ads}	35.4	32.8	15.6	31.6
	$\Delta A^\ddagger_{\mathrm{int}}$	126.5	113.5	117.0	81.9
	$\Delta G^\ddagger_{\mathrm{app}}$	161.9	146.3	132.6	113.5
PBE-D3/harm.[b]	ΔG_{ads}	35.4	33.1	15.8	31.5
	$\Delta A^\ddagger_{\mathrm{int}}$	120.7	108.8	112.9	81.1
	$\Delta G^\ddagger_{\mathrm{app}}$	156.1	141.9	128.7	112.6
RPA/MD (FEPT)	ΔG_{ads}	22.4	23.5	21.5	23.2
	$\Delta A^\ddagger_{\mathrm{int}}$	168.0	161.5	153.5	104.7
	$\Delta G^\ddagger_{\mathrm{app}}$	190.3	185.0	175.0	127.9

[a] Classical vibrational partition function.

[b] Quantum mechanical vibrational partition function.

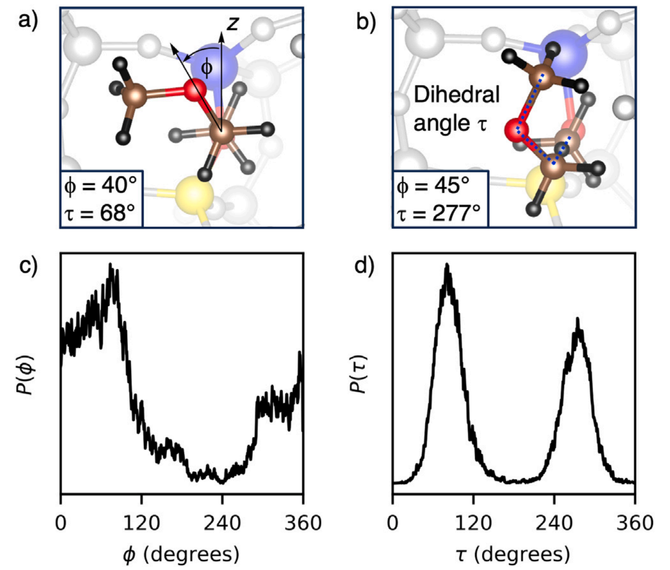

Fig. 5. (a) Atomic structure of the transition state for hydrogen transfer from DME to an SMS (a) and (b) show two harmonic transitions states, i.e. saddle points on the potential energy surface. The rotation of DME is measured by the angle ϕ and is illustrated in (a) The orientation of the terminal CH_3-group is determined by the dihedral angle τ, shown in (b). (c) Probability distribution $P(\phi)$ obtained through MD simulation at the transition state at $\xi = \xi^{\ddagger}$ at 400 °C (d) Same as (b) for $P(\tau)$.

cannot be described by the harmonic approximation. For the transition states, the origin of anharmonicity is less obvious. One degree of freedom we discussed in our previous work [81,82], is the rotation of the substrate (propene and ketene) during methylation by the SMS. A similar situation is observed for the hydrogen transfer reactions and we will discuss this now in detail for DME. The angle ϕ measures the rotation of the methoxy group of DME along the C–C axis determined by other carbon of DME and by the carbon of the SMS. The angle is given relative to the z-axis, as illustrated in Fig. 5(a). For the two obtained saddle points in Fig. 5(a-b), the values of ϕ are 40° and 45°. Fig. 5(c) shows a histogram of ϕ obtained from the MD-simulations. This simulation shows one broad peak ranging from 300° to 360° and continuing from 0° to around 80°, thus describing structures where the methoxy group generally points in positive z-direction.

An additional degree of freedom of the DME moiety in the transition state can be described by the torsional angle C(SMS)-C(DME)-O(DME)-C(DME), as illustrated in Fig. 5(b). The two saddle points in Fig. 5(a-b) show values of τ = 68° and 277°. The distribution obtained from MD in Fig. 5(d) shows two distinct, localized peaks corresponding to values where the methoxy group is oriented roughly orthogonally to the C–C vector determined by the other carbon of DME and by the carbon of the SMS.

We note that the rate with which the system switches between the two orientations defined by the dihedral angle τ depends on the value of the reaction coordinate ξ. At the transition state $\xi^{\ddagger}$ = 1.95 Å during a total simulation time of 354 ps, the methoxy group is in each orientation two times, i.e. it changes back and forth only three times. The same is observed at ξ ≤1.8 Å. At ξ = 1.6 Å the system switches between the two possible orientations more rapidly, approximately six times during 153 ps. The structure with $\tau \approx 90$ ° is also preferred in these cases. At ξ ≤1.4 Å the probability distribution for τ becomes much broader without the distinct states visible for ξ ≥1.6 Å. At the same time, the angle τ changes much more frequently. We thus conclude regarding the orientation of the methoxy group described by τ that different orientations are possible and contribute along the integrated pathway used to determine the activation free energy. In the transition state region, two local minima for τ emerge and rotation between these minima occurs less frequently.

Table 2
Differences in free energies at 400 °C based in on Table 1, given in kJ mol^{-1}.

Method	Quantity	MeOH	DME	DMM	Methyl ketene
Anharmonicity[a]	$\Delta\Delta G_{\mathrm{ads}}$	−23.6	−26.0	−15.6	−25.6
	$\Delta\Delta A^{\ddagger}_{\mathrm{int}}$	7.0	17.1	4.4	11.6
	$\Delta\Delta G^{\ddagger}_{\mathrm{app}}$	−16.7	−8.9	−11.2	−14.1
class−QM[b]	$\Delta\Delta G_{\mathrm{ads}}$	−0.1	0.3	0.3	−0.1
	$\Delta\Delta A^{\ddagger}_{\mathrm{int}}$	−5.7	−4.6	−4.1	−0.8
	$\Delta\Delta G^{\ddagger}_{\mathrm{app}}$	−5.8	−4.4	−3.9	−0.9
RPA−PBE-D3[c]	ΔG_{ads}	10.6	16.7	21.6	17.3
	$\Delta\Delta A^{\ddagger}_{\mathrm{int}}$	34.5	30.9	32.1	11.1
	$\Delta\Delta G^{\ddagger}_{\mathrm{app}}$	45.1	47.6	53.6	28.4

[a] Difference of PBE-D3/MD and PBE-D3/harm. class.
[b] Difference of PBE-D3/harm. class and PBE-D3/harm. QM.
[c] Difference of RPA/MD (FEPT) and PBE-D3/MD.

The results using the harmonic approximation are also listed in Table 1, with the relative and total energy values, with the contributions from the harmonic approximation listed in Tables S13 and S14, respectively. There is a distinct difference of about 5 kJ mol^{-1} in both apparent and intrinsic barriers for hydrogen transfer reactions between the results using the classical and the quantum mechanical vibrational partition function, see Table 2 for differences and Table S9 for free energy values. This is in contrast to adsorption free energies and barriers for methylation, where the same difference is on the order of 1 kJ mol^{-1} or lower. We ascribe this quantum effect to the strong C-H bond that is broken in the transition state and that comes with a high harmonic frequency of around 3000 cm^{-1}.

The adsorption free energies of CO and ketene at an SMS as well as the barriers for the their methylation were taken from our previous work [81,82]. The barrier for methylation of methyl ketene was computed for this work in analogy to Refs. [81,82]. The apparent and intrinsic free energy barriers computed with MD for methyl ketene both at PBE-D3 and RPA (FEPT) level of theory differ by less than 5 kJ mol^{-1} from those obtained previously for ketene.

3.3. Errors of PBE-D3 and the harmonic approximation for adsorption and barriers

Based on the results presented in Table 1 as well as those published previously [81,82] the deviations are listed in Table 2 and visualized in Fig. 6 (the numerical values are shown in Table S1). In our analysis, we refer to the difference between the results obtained with MD simulations and with the harmonic approximation as anharmonicity. However, we note that the difference is also due to using only a single stationary point to apply the harmonic approximation, while the MD simulation in principle samples all accessible space. Focusing first on the error of the harmonic approximation, the results are generally as expected: adsorption is too weak and apparent activation free energies are too high. The error is generally larger for adsorption than for the apparent activation free energies. The anharmonicity for adsorption ranges from around −15 to −25 kJ mol^{-1} without a clear trend among the adsorbates. For transition states, the range is from 0 to −20 kJ mol^{-1}, with no obvious dependence on the type of transition state (methylation or hydrogen transfer). The main outlier is CO-methylation, which has no significant anharmonicity, which can be explained by the lack of additional degrees of freedom in the transition state present for the other substrates.

The difference between RPA and PBE-D3 as obtained through FEPT, is generally of opposite sign, i.e. adsorption is too strong and apparent

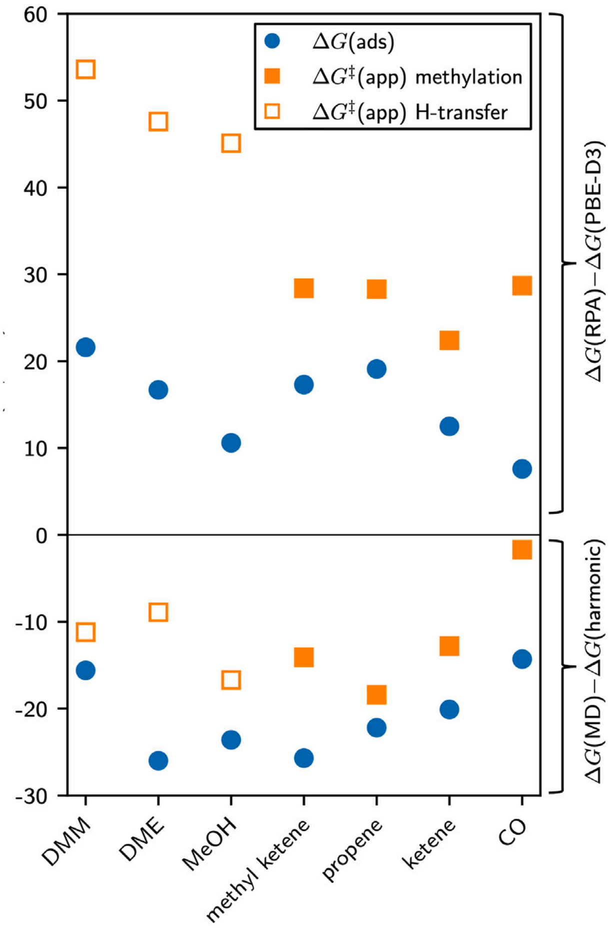

Fig. 6. Overview of errors found for adsorption free energies and activation free energies at 400 °C. Errors of the harmonic approximation (all < 0) and of PBE-D3 (all > 0) are shown in the same graph. The errors of the harmonic approximation are obtained by comparing with the results from the MD-simulations, both at the PBE-D3 level of theory. The errors of PBE-D3 as compared to RPA, are evaluated using FEPT.

activation free energies are too low with PBE-D3. For the error of adsorption, there is a rough correlation with size, as one would expect if dispersion interaction is generally overestimated by PBE-D3. It is noteworthy, that the RPA is expected to slightly underbind,[106] although we expect this error to be smaller in magnitude than that of PBE-D3. Overall, compared to the RPA, PBE-D3 overbinds by 10 to 25 kJ mol^{-1} in adsorption free energies. For apparent activation free energies, there is a clear difference between the two types of reaction. For methylation, the errors are around 30 kJ mol^{-1}, for hydrogen transfer around 50 kJ mol^{-1}.

The adsorption free energies and free energy barriers discussed above and extracted from previous work [81,82] can be considered highly accurate. Both adsorption and barriers are computed with MD simulations. The accuracy is improved to the RPA-level by using FEPT, which is deemed reasonable based on the good overlap as judged by the I_W-Index [96] (see Tables S4 and S10). The RPA itself is generally the most accurate electronic structure method that can still be applied in practice to periodic systems using a plane wave basis set. For reactions in zeolites, we have recently benchmarked the RPA (among other density functionals) for cluster models against DLPNO-CCSD(T) calculations with complete-basis set extrapolated MP2 calculations [37]. We found that the RPA agrees very well, with a mean absolute error of 5 kJ mol^{-1} for the entire test set.

3.4. Free energy profile for initiation

To study the entire reaction pathway for the formation of the first C–C bond, additional calculations were performed in the static approximation, using the harmonic approximation to compute Gibbs free energies and performing single-point energy calculations to compute RPA-corrections. Fig. 7 shows a simplified free energy diagram, where only the highest barrier is shown for some transformations (see Fig. S1 for a scheme containing all computed steps). The simplifications were applied to better visualize the most important aspects, i.e. the highest barriers and most stable intermediates. This can generally be judged by applying the energetic span model [39]. If important minima or transition were omitted, this would generally lead to an underestimation of the energetic span and thus an overestimation of the TOF.

In Fig. 7, calculations performed using MD-simulations are shown in blue, while simulations based on the static approximation are shown in black. The static calculations were kept as they are for two reasons: (1) If barriers are already low in the static approximation, for TS(e-f) and TS(l-m), then they are not expected to be higher if MD simulations were performed and they are in general not expected to be rate-limiting. (2) For gas phase free energy differences without a clear source of anharmonicity (b→c, i2→i, k2→k and l2→l), the static approximation is generally expected to be accurate. Lastly, SMS-formation is not explicitly shown in Fig. 7. Using the static approximation (including a single-point correction based on RPA), we obtain an apparent activation free energy for SMS-formation from clean site (ZOH) and methanol in the gas phase of 165 kJ mol^{-1} for the oxygen considered. This barrier is thus lower than the much higher barrier required for hydrogen transfer and methylation of CO, ketene and methyl ketene by an SMS. Additionally, intermediates like ketene can desorb and react with available SMS either in the same cavity or elsewhere. Consequently, SMS-formation does not necessarily have to occur strictly sequentially at the same active site at which ketene was formed. Therefore, only the free energy difference between ZOH and methanol in the gas phase and the SMS (5 kJ mol^{-1}) are displayed in Fig. 7, for example for intermediate f to g.

Fig. 7 thus shows Gibbs free energies obtained with RPA as the electronic structure method. For all cases that we considered relevant, free energy differences, in particular adsorption, were determined using MD simulations. Starting from DME in the gas phase, the first step is its adsorption, with the aforementioned ΔG_{ads} = 23.6 kJ mol^{-1}. The adsorbed state is here – and in all cases – depicted as a horizontal line, labeled with a '*' above the level of the corresponding gas phase species. Hydrogen transfer from DME to the SMS creates CH_4 and methylated formaldehyde $(CH_2\text{-}O\text{-}CH_3)^+$. Methane readily desorbs, and methylated formaldehyde easily transfers its methyl group back to the zeolite with a low intrinsic free energy barrier of 83 kJ mol^{-1} to give free formaldehyde, which is most stable in the gas phase. The computed apparent free energy for the reaction of DME with an SMS to create CH_4 is 181 kJ mol^{-1}. A similar barrier for the same reaction was estimated based on experimental kinetics to be 193 kJ mol^{-1} in H-ZSM-5 at 748 K [43]. In the same work and at the same conditions we computed a barrier of 212 kJ mol^{-1}[43]. The higher barrier can be explained by the difference in electronic structure method (wave function methods on cluster models vs. RPA), the difference in temperature, the anharmonicity as well as the difference in zeolite catalyst.

Direct hydrogen transfer from formaldehyde to an SMS is rather unfavorable (≈ 250 kJ mol^{-1}) and it is more favorable if formaldehyde first forms an acetal or a hemiacetal [47]. Here, we consider formation of DMM through reaction of formaldehyde with DME, which is (in the gas phase) uphill in Gibbs free energy by 54 kJ mol^{-1}. As described above, the adsorption free energy of DMM at an SMS is 22 kJ mol^{-1} with an intrinsic barrier of 154 kJ mol^{-1} for H-transfer. Overall, hydrogen transfer from DMM to an SMS via TS(c-d) thus has the highest energetic span in Gibbs free energy of 226 kJ mol^{-1} relative to the

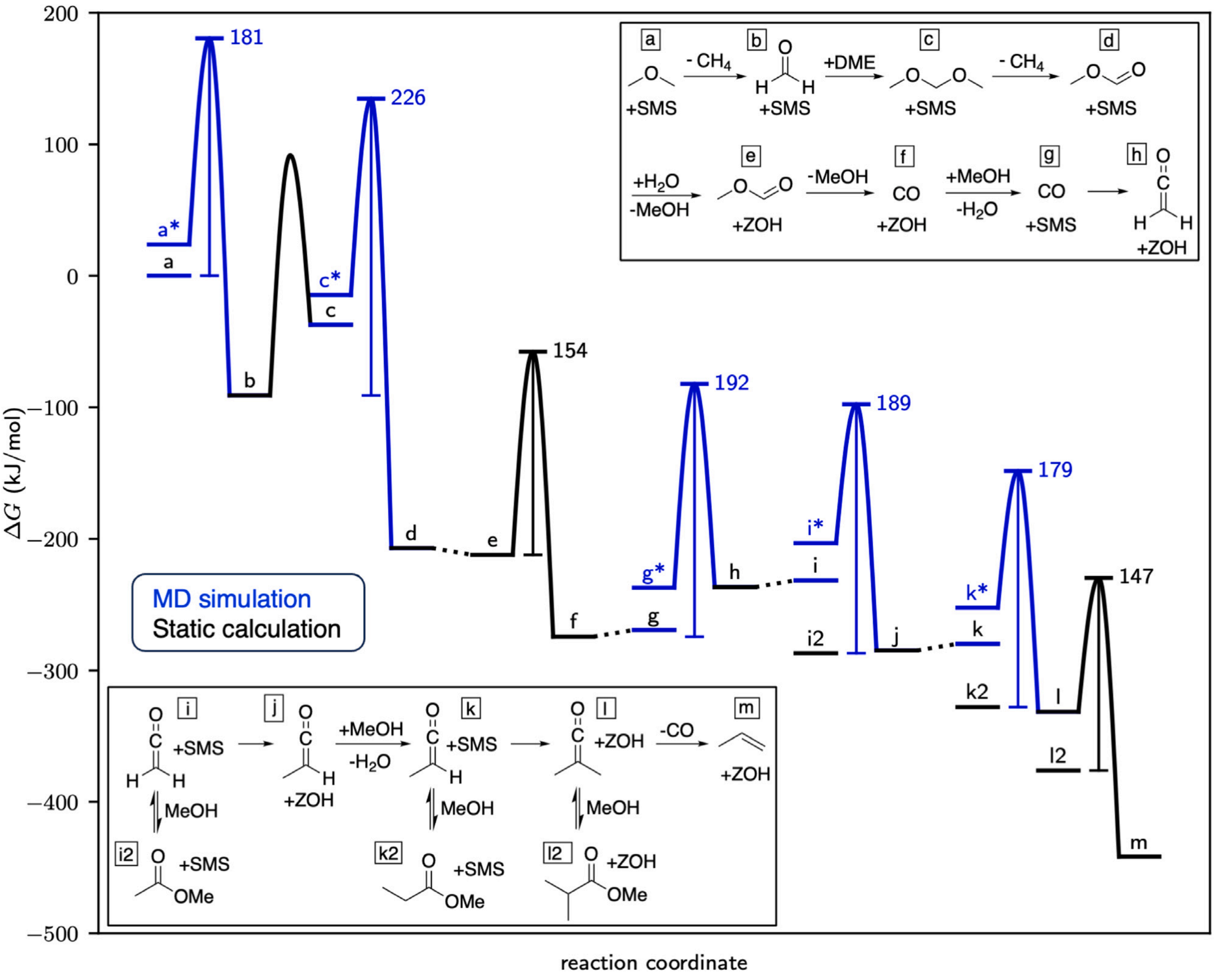

Fig. 7. Simplified Gibbs Free energy diagram at 400 °C and 1 bar reference pressure. Adsorbed molecular states are highlighted with a star "*" in the diagram (a*, c*, g*, i* and k*). In all other cases, the Gibbs free energy of the molecular reactants, intermediates and products refers to the gas phase. The underlying reaction network is shown as an inset and the complete reaction network is given in Fig. S1. Dashed lines are drawn between states where the adsorbate needs to switch from a BAS to an SMS, which can happen either by desorption/adsorption of the adsorbate or by chemical transformation of the active site from BAS to SMS. The formation of the esters (i2, k2 and l2) is a multi-step process, which we assume to be equilibrated.

most stable preceding state, formaldehyde in the gas phase. Computing a rate using the energetic span model would require knowing the partial pressure of formaldehyde, which generally depends on external conditions as well as the reactor setup. However, in previous work we have modeled the initiation kinetics coupled with autocatalytic olefin cycle and have concluded that high barriers are not prohibitive since only small amounts of hydrocarbons need to be formed.

Similar to DME, this hydrogen transfer results in CH_4 and methylated methyl formate $(CH_3\text{-O-CH-O-}CH_3)^+$, which readily transfer a methyl group to the anionic zeolite site to form neutral methyl formate (intrinsic barrier 60 kJ mol^{-1}). Methyl formate decomposes to CO and methanol via TS(e-f) with a moderate activation free energy of 154 kJ mol^{-1}.

CO-methylation requires the formation of an SMS, which is computed to be 5 kJ mol^{-1} uphill from a clean acid site (ZOH). With the previously computed apparent activation free energy of 187 kJ mol^{-1} for TS(g-h), this gives 192 kJ mol^{-1} relative to CO in the gas phase and a clean acid site. The fate of the formed adsorbed ketene, which can be protonated, neutral or adsorbed as surface acetate, has been discussed at length [107]. The rates for ketene protonation to acyl cation and coordination of the acyl cation to the zeolite forming a surface acetyl species are high and these reactions can be considered equilibrated. In the presence of oxygenates such as methanol, the most stable state will be a neutral acetate. Here, we compute that methyl acetate (i2) in the gas phase is 55 kJ mol^{-1} more stable than ketene and methanol in the gas phase (i). Together with the previously computed apparent activation free energy for methylation of ketene via TS(i-j) of 133 kJ mol^{-1}, this gives 189 kJ mol^{-1} relative to methyl acetate in the gas phase. The transition state free energy for formation of methyl acetate is clearly higher than for rearrangement between the other states of ketene, but is 16 kJ mol^{-1} lower than that for ketene methylation towards methyl ketene (Fig. S1). While this difference in barriers will actually likely be somewhat higher due to anharmonicity, it is not large enough to exclude that methyl acetate formation is kinetically limited. This depends of course also on the partial pressure of methanol, but we assume here equilibration with the ester, while noting the relatively small separation of the involved barriers. Overall, limited equilibration with the ester is expected to lead to increased reaction rates for forward methylation, since the esters act as thermodynamic sinks. Since the methylation of the ketenes is not the rate-limiting step for the CO-catalyzed initiation mechanism, the question of equilibration with the esters is not going to change the overall assessment of the mechanism.

Methyl ketene can again form an ester (methyl propionate k2) through reaction with methanol, which we find to be 48 kJ mol^{-1}

more stable in the gas phase. The transition state for the formation of k2 by reaction with methanol is here 21 kJ mol^{-1} lower than that for the forward reaction, methylation towards dimethyl ether. Given the apparent activation free energy of 128 kJ mol^{-1} for methylation of ketene via TS(k-l), this gives 179 kJ mol^{-1} relative to k2. The situation for the formed dimethyl ketene is again analogous, with the neutral ester (l2) being 45 kJ mol^{-1} more stable than dimethyl ketene in the gas phase. The activation free energy for decarbonylation of dimethyl ketene via TS(l-m) is 147 kJ mol^{-1} relative to l2 and therefore too low to be rate limiting. This last step produces propene and thus a free olefin that can build up the hydrocarbon pool through initiation of the autocatalytic olefin cycle.

4. Summary and conclusion

We have computed an anharmonic Gibbs free energy profile for the initiation of the MTO process, starting from DME until the formation of propene. All states were corrected with *ab initio* RPA-calculations, for MD simulations based on FEPT. For the crucial parts, adsorption free energies and activation free energies were computed using MD simulations.

Adsorption at the SMS of the zeolite is weak and positive in Gibbs free energy at 400 °C and 1 bar reference pressure, with MD-computed adsorption free energies in the range of +20 to +30 kJ mol^{-1}. Together with the MD-computed intrinsic free energy barriers, apparent activation free energies can be deduced, which allows to interpret the Gibbs free energy diagrams in terms of the energetic span model, or allows to perform microkinetic modeling. This is not possible with regular MD simulations, as they only provide intrinsic barrier and thus allow no immediate conclusion regarding kinetics.

The harmonic approximation fails badly for adsorption free energies of weakly bound states, with underbinding of around 25 kJ mol^{-1}. For this reason, it is not advisable to combine intrinsic activation free energies from MD simulations with adsorption free energies based on the harmonic approximation in such a case. The harmonic approximation works better for apparent activation free energies and systematically overestimates these with smaller errors ranging from 1.7 to 16.6 kJ mol^{-1}. We note that additional approximations like using only a partial Hessian will likely increase these errors.

PBE-D3 systematically underestimates barriers in zeolites, which is a well-known fact based on static *ab initio* calculations on cluster models. Here we show that this is also the case, when performing *ab initio* calculations directly on periodic models and applying them via FEPT to MD simulations. For methylations, PBE-D3 apparent activation barriers are underestimated by around 25 to 30 kJ mol^{-1}, when compared to RPA. For the hydrogen-transfer reactions, the errors are in the range from 45.1 to 53.6 kJ mol^{-1}.

The energetic span in terms of free energies for the initiation barriers computed here (226 kJ mol^{-1}) is in a similar range as those reported previously, when *ab initio* methods were used [40,47,108]. Low computed barriers for initiation reactions are typically obtained when either intrinsic barriers are reported, or GGA-functionals are used, or both. Kinetic simulations of the autocatalytic initiation process have previously shown that high barriers are not prohibitive for the initiation of the MTO reaction, as only small amounts of olefins need to be generated to initiate the more reactive hydrocarbon pool [40]. What exactly a small amount is cannot be predicted with the chemical intuition that can otherwise be used to understand the steady state reactivity of catalytic cycles based on Gibbs free energy profiles. Instead, this can only be quantified with kinetic simulations that need to include also the autocatalytic part of the hydrocarbon pool reactivity.

The highest barrier of 226 kJ mol^{-1} is found here for the second hydrogen transfer, which leads from formaldehyde to CO. Alternative reactions analogous to the methane-formaldehyde mechanism of formaldehyde with its acetals and hemiacetals have recently been investigated by van Speybroeck and coworkers [46]. In our investigation in 2017 [47], we have studied some of these reactions and found them to be less favorable than the reaction of formaldehyde to CO and then further to ketenes. However, we did not investigate all flavors of the methane-formaldehyde mechanism proposed recently [46] and it remains a future challenge to study these using a high level of electronic structure theory and MD simulations, while accounting for adsorption.

Beyond the initiation of the MTO process discussed here, formaldehyde is also discussed as a reactive intermediate in coke formation [62,65–70]. Here, formaldehyde formed by hydrogen transfer is believed to mainly react in Prins reactions with olefins to eventually form dienes. Our investigation furthermore provides insights into the formation and reaction of ketene, which is also a key intermediate in zeolite catalysis [70,73,78], for example during the initiation mechanism of the MTO process as well as in the OXZEO process [59,60,72].

We expect that the accurate barriers for formation and reactivity of formaldehyde and ketene computed herein will also benefit related research in this area. In future work, we plan to apply the methodology employed here to other important reactions in zeolite catalysis. We expect that this will be particularly interesting for transition states that are loosely bound and which could therefore benefit even more from anharmonicity corrections than those studied here.

CRediT authorship contribution statement

Hector Vicente: Writing – review & editing, Writing – original draft, Validation, Funding acquisition, Data curation. **Philipp N. Plessow:** Writing – review & editing, Writing – original draft, Visualization, Validation, Data curation, Conceptualization.

Declaration of competing interest

The authors declare that they have no known competing financial interests or personal relationships that could have appeared to influence the work reported in this paper.

Acknowledgments

The authors acknowledge support by the state of Baden-Württemberg through bwHPC (bwunicluster and JUSTUS, RV bw17D011) and the German Research Foundation (DFG) through grant no INST 40/575-1 FUGG (JUSTUS 2 cluster). Financial support from the Helmholtz Association, Germany is also gratefully acknowledged. Gefördert durch die Deutsche Forschungsgemeinschaft (DFG) Projektnummer 434253773. H. V. is grateful for his postdoctoral grant from the Basque Government, Spain (POS_2023_1_0018).

Appendix A. Supplementary data

Total energies, Cartesian coordinates and further analysis. MD trajectories were uploaded to a repository [109] to which the Cartesian coordinates of stationary points were also added.

Data availability

Data is provided as supporting information.

References

[1] N. Nesterenko, J. Aguilhon, P. Bodart, D. Minoux, J.P. Dath, Methanol to olefins: An insight into reaction pathways and products formation, Zeolites Zeolite-Like Mater. (2016) 189–263.

[2] W.J. Dehertog, G.F. Froment, Production of light alkenes from methanol on ZSM-5 catalysts, App. Catal. 71 (1) (1991) 153–165.

[3] K. Hemelsoet, J. Van Der Mynsbrugge, K. De Wispelaere, M. Waroquier, V. Van Speybroeck, Unraveling the reaction mechanisms governing methanol-to-olefins catalysis by theory and experiment, ChemPhysChem 14 (8) (2013) 1526–1545.

[4] P. Tian, Y. Wei, M. Ye, Z. Liu, Methanol to olefins (MTO): From fundamentals to commercialization, ACS Catal. 5 (3) (2015) 1922–1938.

[5] M. Bjørgen, S. Svelle, F. Joensen, J. Nerlov, S. Kolboe, F. Bonino, L. Palumbo, S. Bordiga, U. Olsbye, Conversion of methanol to hydrocarbons over zeolite H-ZSM-5: On the origin of the olefinic species, J. Catal. 249 (2) (2007) 195–207.

[6] G. Leonzio, State of art and perspectives about the production of methanol, dimethyl ether and syngas by carbon dioxide hydrogenation, J. CO2 Util. 27 (2018) 326–354.

[7] J. Artz, T.E. Müller, K. Thenert, J. Kleinekorte, R. Meys, A. Sternberg, A. Bardow, W. Leitner, Sustainable conversion of carbon dioxide: An integrated review of catalysis and life cycle assessment, Chem. Rev. 118 (2) (2018) 434–504.

[8] I.U. Din, M.S. Shaharun, M.A. Alotaibi, A.I. Alharthi, A. Naeem, Recent developments on heterogeneous catalytic CO2 reduction to methanol, J. CO2 Util. 34 (2019) 20–33.

[9] N.D. Nielsen, A.D. Jensen, J.M. Christensen, The roles of CO and CO2 in high pressure methanol synthesis over cu-based catalysts, J. Catal. 393 (2021) 324–334.

[10] P. Battaglia, G. Buffo, D. Ferrero, M. Santarelli, A. Lanzini, Methanol synthesis through CO2 capture and hydrogenation: Thermal integration, energy performance and techno-economic assessment, J. CO2 Util. 44 (2021) 101407.

[11] T. Cordero-Lanzac, A. Ramirez, A. Navajas, L. Gevers, S. Brunialti, L.M. Gandía, A.T. Aguayo, S. Mani Sarathy, J. Gascon, A techno-economic and life cycle assessment for the production of green methanol from CO2: catalyst and process bottlenecks, J. Energy Chem. 68 (2022) 255–266.

[12] H.O. LeClerc, H.C. Erythropel, A. Backhaus, D.S. Lee, D.R. Judd, M.M. Paulsen, M. Ishii, A. Long, L. Ratjen, G. Gonsalves Bertho, C. Deetman, Y. Du, M.K.M. Lane, P.V. Petrovic, A.T. Champlin, A. Bordet, N. Kaeffer, G. Kemper, J.B. Zimmerman, W. Leitner, P.T. Anastas, The CO2 tree: The potential for carbon dioxide utilization pathways, ACS Sustain. Chem. Eng. 13 (1) (2025) 5–29.

[13] N. Yusuf, F. Almomani, Highly effective hydrogenation of CO2 to methanol over Cu/ZnO/Al2O3 catalyst: A process economy & environmental aspects, Fuel 332 (2023) 126027.

[14] A.S. Al-Dughaither, H. de Lasa, Neat dimethyl ether conversion to olefins (DTO) over HZSM-5: Effect of SiO2/Al2O3 on porosity, surface chemistry, and reactivity, Fuel 138 (2014) 52–64.

[15] T. Cordero-Lanzac, A.G. Gayubo, A.T. Aguayo, J. Bilbao, The MTO and DTO processes as greener alternatives to produce olefins: A review of kinetic models and reactor design, Chem. Eng. J. 494 (2024) 152906.

[16] I.M. Dahl, S. Kolboe, On the reaction mechanism for propene formation in the MTO reaction over SAPO-34, Catal. Lett. 20 (3) (1993) 329–336.

[17] I.M. Dahl, S. Kolboe, On the reaction mechanism for hydrocarbon formation from methanol over SAPO-34: I. isotopic labeling studies of the Co-reaction of ethene and methanol, J. Catal. 149 (2) (1994) 458–464.

[18] I.M. Dahl, S. Kolboe, On the reaction mechanism for hydrocarbon formation from methanol over SAPO-34: 2. isotopic labeling studies of the Co-reaction of propene and methanol, J. Catal. 161 (1) (1996) 304–309.

[19] S. Svelle, F. Joensen, J. Nerlov, U. Olsbye, K.-P. Lillerud, S. Kolboe, M. Bjørgen, Conversion of methanol into hydrocarbons over zeolite H-ZSM-5:Ethene formation is mechanistically separated from the formation of higher alkenes, J. Am. Chem. Soc. 128 (46) (2006) 14770–14771.

[20] M. Westgård Erichsen, S. Svelle, U. Olsbye, The influence of catalyst acid strength on the methanol to hydrocarbons (MTH) reaction, Catal. Today 215 (2013) 216–223.

[21] U. Olsbye, S. Svelle, M. Bjorgen, P. Beato, T.V. Janssens, F. Joensen, S. Bordiga, K.P. Lillerud, Conversion of methanol to hydrocarbons: how zeolite cavity and pore size controls product selectivity, Angew. Chem. Int. Ed. Engl. 51 (24) (2012) 5810–5831.

[22] V. Van Speybroeck, K. De Wispelaere, J. Van der Mynsbrugge, M. Vandichel, K. Hemelsoet, M. Waroquier, First principle chemical kinetics in zeolites: the methanol-to-olefin process as a case study, Chem. Soc. Rev. 43 (21) (2014) 7326–7357.

[23] J.F. Haw, W. Song, D.M. Marcus, J.B. Nicholas, The mechanism of methanol to hydrocarbon catalysis, Acc. Chem. Res. 36 (5) (2003) 317–326.

[24] V. Van Speybroeck, K. Hemelsoet, L. Joos, M. Waroquier, R.G. Bell, C.R. Catlow, Advances in theory and their application within the field of zeolite chemistry, Chem. Soc. Rev. 44 (20) (2015) 7044–7111.

[25] I. Yarulina, A.D. Chowdhury, F. Meirer, B.M. Weckhuysen, J. Gascon, Recent trends and fundamental insights in the methanol-to-hydrocarbons process, Nat. Catal. 1 (6) (2018) 398–411.

[26] V. Van Speybroeck, M. Bocus, P. Cnudde, L. Vanduyfhuys, Operando modeling of zeolite-catalyzed reactions using first-principles molecular dynamics simulations, ACS Catal. 13 (17) (2023) 11455–11493, http://dx.doi.org/10.1021/acscatal.3c01945.

[27] C. Chizallet, C. Bouchy, K. Larmier, G. Pirngruber, Molecular views on mechanisms of bronsted acid-catalyzed reactions in zeolites, Chem. Rev. 123 (9) (2023) 6107–6196, http://dx.doi.org/10.1021/acs.chemrev.2c00896.

[28] S. Lin, H. Li, P. Tian, Y. Wei, M. Ye, Z. Liu, Methanol to olefins (MTO): Understanding and regulating dynamic complex catalysis, J. Am. Chem. Soc. 147 (14) (2025) 11585–11607, http://dx.doi.org/10.1021/jacs.4c12145.

[29] D. Lesthaeghe, V. Van Speybroeck, G.B. Marin, M. Waroquier, The rise and fall of direct mechanisms in methanol-to-olefin catalysis: An overview of theoretical contributions, Ind. Eng. Chem. Res. 46 (26) (2007) 8832–8838.

[30] D. Lesthaeghe, V. Van Speybroeck, G.B. Marin, M. Waroquier, Understanding the failure of direct C-C coupling in the zeolite-catalyzed methanol-to-olefin process, Angew. Chem. Int. Ed. 45 (11) (2006) 1714–1719.

[31] W. Song, D.M. Marcus, H. Fu, J.O. Ehresmann, J.F. Haw, An oft-studied reaction that may never have been: Direct catalytic conversion of methanol or dimethyl ether to hydrocarbons on the solid acids HZSM-5 or HSAPO-34, J. Am. Chem. Soc. 124 (2002).

[32] J. Amsler, P.N. Plessow, F. Studt, Effect of impurities on the initiation of the methanol-to-olefins process: Kinetic modeling based on Ab initio rate constants, Catal. Lett. 151 (9) (2021) 2595–2602.

[33] S. Svelle, C. Tuma, X. Rozanska, T. Kerber, J. Sauer, Quantum chemical modeling of zeolite-catalyzed methylation reactions: Toward chemical accuracy for barriers, J. Am. Chem. Soc. 131 (2) (2009) 816–825.

[34] J. Sauer, The future of computational catalysis, J. Catal. 433 (2024).

[35] J. Sauer, Ab initio calculations for molecule-surface interactions with chemical accuracy, Acc. Chem. Res. 52 (12) (2019) 3502–3510.

[36] T.J. Goncalves, P.N. Plessow, F. Studt, On the accuracy of density functional theory in zeolite catalysis, ChemCatChem 11 (17) (2019) 4368–4376.

[37] P. Huber, P.N. Plessow, Accurate and efficient description of acidic zeolites with plane-wave density functional theory using range-separated hybrid functionals, ChemPhysChem 26 (15) (2025) e202500147.

[38] M. Bocus, S. Vandenhaute, V. Van Speybroeck, The operando nature of isobutene adsorbed in zeolite H-SSZ-13 unraveled by machine learning potentials beyond DFT accuracy, Angew. Chem. Int. Ed. Engl. (2024) e202413637.

[39] S. Kozuch, S. Shaik, How to conceptualize catalytic cycles? The energetic span model, Acc. Chem. Res. 44 (2) (2011) 101–110.

[40] P.N. Plessow, A. Smith, S. Tischer, F. Studt, Identification of the reaction sequence of the MTO initiation mechanism using Ab initio-based kinetics, J. Am. Chem. Soc. 141 (14) (2019) 5908–5915.

[41] N. Tajima, T. Tsuneda, F. Toyama, K. Hirao, A new mechanism for the first carbon-carbon bond formation in the MTG process: A theoretical study, J. Am. Chem. Soc. 120 (32) (1998) 8222–8229.

[42] J.E. Jackson, F.M. Bertsch, Conversion of methanol to gasoline: new mechanism for formation of the first carbon-carbon bond, J. Am. Chem. Soc. 112 (25) (1990) 9085–9092.

[43] F.M. Kirchberger, Y. Liu, P.N. Plessow, M. Tonigold, F. Studt, M. Sanchez-Sanchez, J.A. Lercher, Mechanistic differences between methanol and dimethyl ether in zeolite-catalyzed hydrocarbon synthesis, Proc. Natl. Acad. Sci. 119 (4) (2022) e2103840119.

[44] J. Li, Z. Wei, Y. Chen, B. Jing, Y. He, M. Dong, H. Jiao, X. Li, Z. Qin, J. Wang, W. Fan, A route to form initial hydrocarbon pool species in methanol conversion to olefins over zeolites, J. Catal. 317 (2014) 277–283.

[45] Z. Wei, Y.-Y. Chen, J. Li, W. Guo, S. Wang, M. Dong, Z. Qin, J. Wang, H. Jiao, W. Fan, Stability and reactivity of intermediates of methanol related reactions and C–C bond formation over H-ZSM-5 acidic catalyst: A computational analysis, J. Phys. Chem. C 120 (11) (2016) 6075–6087.

[46] W. Chen, J. Sobalska, W. Fu, K.A. Tarach, M. Bocus, T. Tang, K. Góra-Marek, V. Van Speybroeck, Formaldehyde-mediated initial carbon–carbon bond formation in zeolite-catalyzed methanol-to-hydrocarbon conversion, J. Am. Chem. Soc. 147 (28) (2025) 24719–24733.

[47] P.N. Plessow, F. Studt, Unraveling the mechanism of the initiation reaction of the methanol to olefins process using ab initio and DFT calculations, ACS Catal. 7 (11) (2017) 7987–7994.

[48] W. Wang, M. Hunger, Reactivity of surface alkoxy species on acidic zeolite catalysts, Acc. Chem. Res. 41 (8) (2008) 895–904, http://dx.doi.org/10.1021/ar700210f.

[49] P. Cheung, A. Bhan, G.J. Sunley, E. Iglesia, Selective carbonylation of dimethyl ether to methyl acetate catalyzed by acidic zeolites, Angew. Chem. Int. Ed. Engl. 45 (10) (2006) 1617–1620.

[50] A. Bhan, A.D. Allian, G.J. Sunley, D.J. Law, E. Iglesia, Specificity of sites within eight-membered ring zeolite channels for carbonylation of methyls to acetyls, J. Am. Chem. Soc. 129 (16) (2007) 4919–4924.

[51] M. Lusardi, T.T. Chen, M. Kale, J.H. Kang, M. Neurock, M.E. Davis, Carbonylation of dimethyl ether to methyl acetate over SSZ-13, ACS Catal. 10 (1) (2020) 842–851, http://dx.doi.org/10.1021/acscatal.9b04307.

[52] A.D. Chowdhury, K. Houben, G.T. Whiting, M. Mokhtar, A.M. Asiri, S.A. Al-Thabaiti, S.N. Basahel, M. Baldus, B.M. Weckhuysen, Initial carbon–carbon bond formation during the early stages of the methanol-to-olefin process proven by zeolite-trapped acetate and methyl acetate, Angew. Chem. 128 (51) (2016) 16072–16077.

[53] J. S. Martinez-Espin, M. Mortén, T.V. W. Janssens, S. Svelle, P. Beato, U. Olsbye, New insights into catalyst deactivation and product distribution of zeolites in the methanol-to-hydrocarbons (MTH) reaction with methanol and dimethyl ether feeds, Catal. Sci. Technol. 7 (13) (2017) 2700–2716.

[54] G.J. Hutchings, F. Gottschalk, M.V.M. Hall, R. Hunter, Hydrocarbon formation from methylating agents over the zeolite catalyst ZSM-5. comments on the mechanism of carbon–carbon bond and methane formation, J. Chem. Soc. Faraday Trans. 1 83 (3) (1987) 571–583.

[55] A. Comas-Vives, M. Valla, C. Copéret, P. Sautet, Cooperativity between Al sites promotes hydrogen transfer and carbon–carbon bond formation upon dimethyl ether activation on alumina, ACS Cent. Sci. 1 (6) (2015) 313–319.

[56] Y. Liu, S. Müller, D. Berger, J. Jelic, K. Reuter, M. Tonigold, M. Sanchez-Sanchez, J.A. Lercher, Formation mechanism of the first carbon–carbon bond and the first olefin in the methanol conversion into hydrocarbons, Angew. Chem. Int. Ed. 55 (19) (2016) 5723–5726.

[57] G.J. Hutchings, F. Gottschalk, R. Hunter, Comments on “kinetic model for methanol conversion to olefins” with respect to methane formation at low conversion, Ind. Eng. Chem. Res. 27 (1987) 637–638.

[58] L. Yang, T. Yan, C. Wang, W. Dai, G. Wu, M. Hunger, W. Fan, Z. Xie, N. Guan, L. Li, Role of acetaldehyde in the roadmap from initial carbon–carbon bonds to hydrocarbons during methanol conversion, ACS Catal. 9 (7) (2019) 6491–6501.

[59] F. Jiao, J. Li, X. Pan, J. Xiao, H. Li, H. Ma, M. Wei, Y. Pan, Z. Zhou, M. Li, S. Miao, J. Li, Y. Zhu, D. Xiao, T. He, J. Yang, F. Qi, Q. Fu, X. Bao, Selective conversion of syngas to light olefins, Science 351 (6277) (2016) 1065–1068.

[60] F. Jiao, X. Pan, K. Gong, Y. Chen, G. Li, X. Bao, Shape-selective zeolites promote ethylene formation from syngas via a ketene intermediate, Angew. Chem. Int. Ed. Engl. 57 (17) (2018) 4692–4696.

[61] X. Wu, Z. Zhang, Z. Pan, X. Zhou, A. Bodi, P. Hemberger, Ketenes in the induction of the methanol-to-olefins process, Angew. Chem. Int. Ed. 61 (41) (2022) e202207777.

[62] Y. Liu, F.M. Kirchberger, S. Müller, M. Eder, M. Tonigold, M. Sanchez-Sanchez, J.A. Lercher, Critical role of formaldehyde during methanol conversion to hydrocarbons, Nat. Commun. 10 (1) (2019) 1462.

[63] P. Huber, P.N. Plessow, A computational investigation of the decomposition of acetic acid in H-SSZ-13 and its role in the initiation of the MTO process, Catal. Sci. Technol. 13 (6) (2023) 1905–1917.

[64] P. Huber, P.N. Plessow, The role of decarboxylation reactions during the initiation of the methanol-to-olefins process, J. Catal. 428 (2023) 115134.

[65] S. Muller, Y. Liu, F.M. Kirchberger, M. Tonigold, M. Sanchez-Sanchez, J.A. Lercher, Hydrogen transfer pathways during zeolite catalyzed methanol conversion to hydrocarbons, J. Am. Chem. Soc. 138 (49) (2016) 15994–16003, http://dx.doi.org/10.1021/jacs.6b09605.

[66] A. Hwang, A. Bhan, Deactivation of zeolites and zeotypes in methanol-to-hydrocarbons catalysis: Mechanisms and circumvention, Acc. Chem. Res. 52 (9) (2019) 2647–2656.

[67] B.L. Foley, B.A. Johnson, A. Bhan, Kinetic evaluation of deactivation pathways in methanol-to-hydrocarbon catalysis on HZSM-5 with formaldehyde, olefinic, dieneic, and aromatic Co-feeds, ACS Catal. 11 (6) (2021) 3628–3637.

[68] C.W.P. Pare, P. Rzepka, P. Hemberger, A. Bodi, R. Hauert, J.A. van Bokhoven, V. Paunović, Formaldehyde-induced deactivation of ZSM5 catalysts during the methanol-to-hydrocarbons conversion, ACS Catal. 14 (1) (2024) 463–474.

[69] J. Luo, T. Xiao, C. Liu, Y. Pan, Recent progress on the involvement of formaldehyde in the methanol-to-hydrocarbons reaction, ChemSusChem 18 (2) (2025) e202400884.

[70] V. Paunović, X. Wu, L. Maggiulli, D. Ferri, P. Hemberger, A. Bodi, J.A.v. Bokhoven, The formation, reactivity and transformation pathways of formaldehyde in the methanol-to-hydrocarbon conversion, Catal. Sci. Technol. 14 (5) (2024) 1216–1228.

[71] V. Paunović, P. Hemberger, A. Bodi, R. Hauert, J.A. van Bokhoven, Impact of nonzeolite-catalyzed formation of formaldehyde on the methanol-to-hydrocarbons conversion, ACS Catal. 12 (21) (2022) 13426–13434.

[72] X. Pan, F. Jiao, D. Miao, X. Bao, Oxide-zeolite-based composite catalyst concept that enables syngas chemistry beyond fischer-tropsch synthesis, Chem. Rev. 121 (11) (2021) 6588–6609.

[73] D. Xiong, Z. Lai, J. Chen, H. Yuan, H. Wang, Ketene conversion chemistry within mordenite zeolite: Pore-size-dependent reaction mechanism, product selectivity, and catalytic activity, J. Am. Chem. Soc. 147 (20) (2025) 17303–17314.

[74] Y. Zhang, P. Gao, F. Jiao, Y. Chen, Y. Ding, G. Hou, X. Pan, X. Bao, Chemistry of ketene transformation to gasoline catalyzed by H-SAPO-11, J. Am. Chem. Soc. 144 (40) (2022) 18251–18258.

[75] Z. Guo, Q. Chen, J. Liu, B. Yang, Discovery of ketene/acetyl as a potential receptor for hydrogen-transfer reactions in zeolites, Nat. Commun. 16 (1) (2025) 1152, http://dx.doi.org/10.1038/s41467-024-55514-1.

[76] W. Chen, P. Cnudde, V.V. Speybroeck, Understanding the entanglement between diffusion and reaction by probing the mobility of ketene in chabazites, J. Catal. (2025) http://dx.doi.org/10.1016/j.jcat.2025.116546.

[77] Q. Chen, J. Liu, B. Yang, Resolving the relations between methanol and ketene/acetyl within HSAPO-34 in the bifunctional syngas-to-olefin process, ACS Catal. 15 (12) (2025) 10796–10807.

[78] W. Chen, P. Cnudde, A minireview to ketene chemistry in zeolite catalysis, Chin. J. Struct. Chem. 43 (11) (2024) 100412.

[79] A.D. Chowdhury, J. Gascon, The curious case of ketene in zeolite chemistry and catalysis, Angew. Chem. Int. Ed. Engl. 57 (46) (2018) 14982–14985, http://dx.doi.org/10.1002/anie.201808480.

[80] C.M. Wang, Y.D. Wang, Z.K. Xie, Methylation of olefins with ketene in zeotypes and its implications for the direct conversion of syngas to light olefins: a periodic DFT study, Catal. Sci. Technol. 6 (17) (2016) 6644–6649, http://dx.doi.org/10.1039/c6cy01095d.

[81] P.N. Plessow, Anharmonic adsorption free energies and apparent activation barriers for mobile reactants based on molecular dynamics simulations, J. Chem. Theory Comput. 21 (17) (2025) 8518–8532.

[82] P.N. Plessow, Correction to “anharmonic adsorption free energies and apparent activation barriers for mobile reactants based on molecular dynamics simulations”, J. Chem. Theory Comput. 21 (22) (2025) http://dx.doi.org/10.1021/acs.jctc.5c01826, 11820–11820.

[83] J.P. Perdew, Generalized gradient approximation made simple, Phys. Rev. Lett. 77 (18) (1996) 3865–3868.

[84] S. Grimme, J. Antony, S. Ehrlich, H. Krieg, A consistent and accurate ab initio parametrization of density functional dispersion correction (DFT-D) for the 94 elements H-Pu, J. Chem. Phys. 132 (15) (2010) 154104.

[85] P.E. Blöchl, Projector augmented-wave method, Phys. Rev. B 50 (24) (1994) 17953–17979.

[86] G. Kresse, J. Furthmüller, Efficient iterative schemes for ab initio total-energy calculations using a plane-wave basis set, Phys. Rev. B 54 (16) (1996) 11169–11186.

[87] G. Kresse, D. Joubert, From ultrasoft pseudopotentials to the projector augmented-wave method, Phys. Rev. B 59 (3) (1999) 1758–1775.

[88] M.E. Tuckerman, Statistical Mechanics: Theory and Molecular Simulation, Oxford University Press, 2023.

[89] E.A. Carter, G. Ciccotti, J.T. Hynes, R. Kapral, Constrained reaction coordinate dynamics for the simulation of rare events, Chem. Phys. Lett. 156 (5) (1989) 472–477.

[90] J. Rey, C. Bignaud, P. Raybaud, T. Bučko, C. Chizallet, Dynamic features of transition states for β-scission reactions of alkenes over acid zeolites revealed by AIMD simulations, Angew. Chem. 132 (43) (2020) 19100–19104.

[91] M. Gešvandtnerová, P. Raybaud, C. Chizallet, T. Bučko, Importance of dynamic effects in isobutanol to linear butene conversion catalyzed by acid zeolites assessed by AIMD, ACS Catal. 14 (10) (2024) 7478–7491.

[92] L. Benco, T. Bucko, J. Hafner, Activity and reactivity of Fe2+ cations in the zeolite. Ab initio free-energy MD calculation of the N2O dissociation over iron-exchanged ferrierite, J. Phys. Chem. C 113 (43) (2009) 18807–18816.

[93] S.K. Schiferl, D.C. Wallace, Statistical errors in molecular dynamics averages, J. Chem. Phys. 83 (10) (1985) 5203–5209.

[94] H. Flyvbjerg, H.G. Petersen, Error estimates on averages of correlated data, J. Chem. Phys. 91 (1) (1989) 461–466.

[95] M. Kaltak, Cubic scaling algorithm for the random phase approximation: Self-interstitials and vacancies in Si, Phys. Rev. B 90 (5) (2014).

[96] T. Bučko, M. Gešvandtnerová, D. Rocca, Ab initio calculations of free energy of activation at multiple electronic structure levels made affordable: An effective combination of perturbation theory and machine learning, J. Chem. Theory Comput. 16 (10) (2020) 6049–6060.

[97] J. Rey, C. Chizallet, D. Rocca, T. Bucko, M. Badawi, Reference-quality free energy barriers in catalysis from machine learning thermodynamic perturbation theory, Angew. Chem. Int. Ed. Engl. 63 (6) (2024) e202312392.

[98] B. Chehaibou, M. Badawi, T. Bucko, T. Bazhirov, D. Rocca, Computing RPA adsorption enthalpies by machine learning thermodynamic perturbation theory, J. Chem. Theory Comput. 15 (11) (2019) 6333–6342.

[99] J. Rey, M. Badawi, D. Rocca, C. Chizallet, T. Bučko, Machine learning thermodynamic perturbation theory offers accurate activation free energies at the RPA level for alkene isomerization in zeolites, Catal. Sci. Technol. 14 (18) (2024) 5314–5323.

[100] B. Widom, Potential-distribution theory and the statistical mechanics of fluids, J. Phys. Chem. 86 (6) (1982) 869–872, http://dx.doi.org/10.1021/j100395a005.

[101] B. Widom, Some topics in the theory of fluids, J. Chem. Phys. 39 (11) (1963) 2808–2812, http://dx.doi.org/10.1063/1.1734110.

[102] B. Smit, Molecular simulations of zeolites: Adsorption, diffusion, and shape selectivity, Chem. Rev. 108 (10) (2008) 4125–4184, http://dx.doi.org/10.1021/cr8002642.

[103] C.H. Bennett, Efficient estimation of free energy differences from Monte Carlo data, J. Comput. Phys. 22 (2) (1976) 245–268.

[104] G. Konig, S. Bruckner, S. Boresch, Unorthodox uses of Bennett’s acceptance ratio method, J. Comput. Chem. 30 (11) (2009) 1712–1718, http://dx.doi.org/10.1002/jcc.21255, URL https://www.ncbi.nlm.nih.gov/pubmed/19373838.

[105] T. Bucko, S. Chibani, J.F. Paul, L. Cantrel, M. Badawi, Dissociative iodomethane adsorption on Ag-MOR and the formation of AgI clusters: an ab initio molecular dynamics study, Phys. Chem. Chem. Phys. 19 (40) (2017) 27530–27543, http://dx.doi.org/10.1039/c7cp05562e.

[106] J. Klimes, D.P. Tew, Efficient and accurate description of adsorption in zeolites, J. Chem. Phys. 151 (23) (2019) 234108.

[107] W. Chen, G. Li, X. Yi, S.J. Day, K.A. Tarach, Z. Liu, S.B. Liu, S.C. Edman Tsang, K. Gora-Marek, A. Zheng, Molecular understanding of the catalytic consequence of ketene intermediates under confinement, J. Am. Chem. Soc. 143 (37) (2021) 15440–15452, http://dx.doi.org/10.1021/jacs.1c08036.

[108] M. Fečík, P.N. Plessow, F. Studt, Theoretical investigation of the side-chain mechanism of the MTO process over H-SSZ-13 using DFT and ab initio calculations, Catal. Sci. Technol. 11 (11) (2021) 3826–3833, http://dx.doi.org/10.1039/d1cy00433f.

[109] P.N. Plessow, 2025. http://dx.doi.org/10.35097/dtw6h3v9bfkfrj6n. https://radar.kit.edu/radar/de/dataset/dtw6h3v9bfkfrj6n#.